Neoclassical Computation of Temperature Anisotropy in the National Spherical Torus Experiment

David Perkins

A senior thesis submitted to the faculty of
Brigham Young University
in partial fulfillment of the requirements for the degree of

Bachelor of Science

Ross Spencer, Advisor

Department of Physics and Astronomy

Brigham Young University

April 2013

ABSTRACT

Neoclassical Computation of Temperature Anisotropy
in the National Spherical Torus Experiment

David Perkins
Department of Physics and Astronomy
Bachelor of Science

The National Spherical Torus Experiment (NSTX), underway at Princeton Plasma Physics Laboratory (PPPL), investigates the plasma dynamics in a spherical tokamak to understand the device's potential as a fusion power generator. Temperature anisotropy, a characteristic that could have substantial effects on the plasma's overall dynamics, is not well-known in NSTX. The particle code GTC-NEO, a particle-in-cell simulation developed at PPPL, allows for computational diagnosis of temperature anisotropy. The code simulates a tokamak plasma in the neoclassical limit. We present herein a computational study of temperature anisotropy in NSTX using GTC-NEO, including spatial temperature anisotropy profiles in varied regimes of particle collision frequency. Results show that anisotropy is less than 5% in NSTX. We observed that temperature anisotropy peaks near the edge of the plasma on the outboard side of the device. The magnitude of this peak varies inversely with collision frequency.

Keywords: Temperature Anisotropy, NSTX, Neoclassical Transport, Nuclear Fusion Power

ACKNOWLEDGMENTS

I wish to acknowledge the ongoing support of Stephane Ethier and Weixing Wang of Princeton Plasma Physics Lab. This thesis began as a summer internship project and Drs. Ethier and Wang were kind enough to act as my continuing advisors following the completion of the program. I would further like to thank my BYU advisor, Dr. Ross Spencer, for offering invaluable help and advice despite being unconnected to the project. Many mistakes were avoided or rectified thanks to his careful supervision.

Contents

List of Figures

Chapter 1

Introduction: Temperature Anisotropy in the National Spherical Torus Experiment

1.1 Magnetic Confinement Fusion

Nuclear fusion is an attractive potential source of clean energy. The abundance of fuel and the comparative innocuity of its by-products—not to mention its ample yield—render fusion among the most promising of future solutions for sustainable energy. In this section we present a very brief discussion of magnetic confinement fusion; more information can be found in any text on fusion energy, such as [1].

For fusion to occur, two small nuclei must be brought within the range of the strong nuclear force. Such can only occur if the nuclei are energetic enough to overcome the longer-range mutual Coulombic repulsion that occurs due to their net positive charges. Indeed, a sustained fusion reaction can only occur if the fuel is a plasma—the most energetic state of matter. While some approaches to fusion energy focus on pulsed reactions [2], which can in principle occur with fuel in an initially less energetic state, we examine an approach that seeks for a sustained reaction.

Fusion plasmas cannot be reasonably contained in the same way as a cool gas. No solid container can withstand the extreme temperature of a fusion plasma. Furthermore, contact with container walls would cool the plasma far too much to allow the plasma to maintain the high internal energy required for fusion. However, since plasmas consist of dissociated electrons and ions, both having nonzero charges, a plasma can be confined to a finite space with a judiciously arranged magnetic field. In general, modern devices for fusion plasma confinement form the plasma into a torus, since it is possible for a magnetic field to be everywhere nonzero and tangent to a toroidal surface (a property vital to the sustained confinement of plasma). We clarify that in discussing a torus in this paper, we refer to a solid torus; in reference to the geometric surface, we shall use the term "toroidal surface" to avoid abiguity. The most common magnetic confinement device of this variety is known as the tokamak. The tokamak has a simple toroidal geometry and relies on external field coils as well as currents within the plasma to generate the magnetic field necessary for confinement.

Though nuclear fusion has been achieved in magnetic confinement devices, it is not yet a viable source of energy due to issues of reaction sustainability and high energy input requirements [3]. Since fusion power has strong potential, it is wise to explore fully the various possibilities that could lead to successful and economical fusion power generation. Furthermore, it is necessary to understand the dynamics of a magnetically confined plasma, and in particular the transport of particles and energy through magnetically confined systems. These are the subjects of much ongoing research [1]. This thesis is focused on an important element of this research, measuring temperature anisotropy in a tokamak.

1.2 Particle Transport and Toroidal Particle Dynamics

In magnetic confinement fusion, understanding the transport of particles and energy through the plasma is of the utmost importance, for transport is the mechanism of energy loss that prevents sustained fusion [1]. In this thesis we focus on effects of particle transport. Particle transport results from various mechanisms, which can be lumped into three main categories of transport theory: classical transport, neoclassical transport, and turbulent transport. We shall be primarily concerned with neoclassical transport theory, but we discuss all three briefly in this section. For further resources on transport, see [4, 5].

Classical transport is an idealized view of particle diffusion through the plasma as a result of collisions with other particles. In the simplest view of a magnetized plasma, particles gyrate in small circular orbits as they move along magnetic field lines (see Appendix A). If two particles collide, their trajectories change; however, they remain in orbits with gyroradii comparable to the original. As a result, a single collision will not cause a particle's trajectory to shift by more than roughly a particle gyroradius. This means that the collisional step size for classical transport is on the order of the particle gyroradius, which is normally small compared with the overall tokamak geometry. In general, classical transport theory is not valid for examining a toroidally confined plasma; neoclassical transport theory must be used instead.

Neoclassical transport is an adaptation of classical transport to take into account toroidal particle dynamics. These dynamics describe the geometric effects of toroidal magnetic fields on particle motion (see Appendix A). This motion includes particle drift and other effects, which lead to some important predictions. Most prominently, a portion of particles will become trapped in banana orbits, in which the particles become confined to a specific radial and poloidal range in the plasma (see Fig. 1.1). This occurs because the magnetic field strength increases as the particle moves from the outboard side of the torus to the inboard side. As described in Appendix A, this causes the magnetic mirror effect, reversing the particle's direction of motion parallel to the magnetic field. As

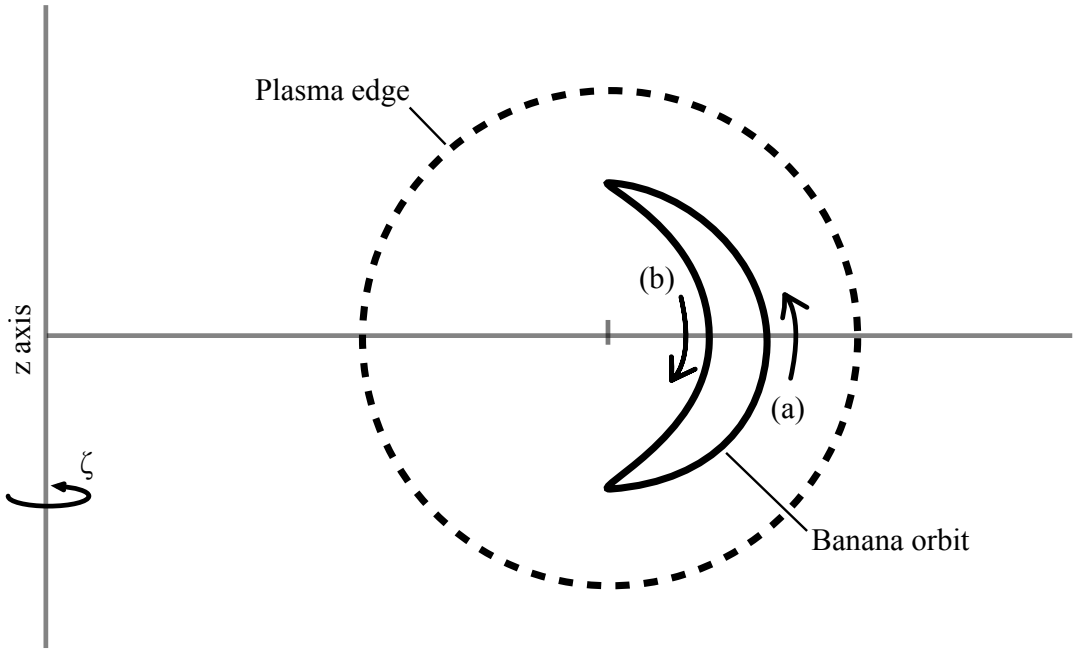

Figure 1.1 Toroidal cross-section showing a banana orbit. A particle trapped in a banana orbit follows trajectory (a) while moving in the $+\zeta$ direction (into the page), then slows to a stop and reverses direction to move along trajectory (b) in the $-\zeta$ direction (out of the page).

shown in Fig. 1.1, the particle moves back and forth between two mirrors, but along two different trajectories. The distance between these paths is called the banana width. Whereas the characteristic step size of classical transport is the gyroradius, as described above, the banana width forms the characteristic step size for neoclassical transport by an analogous process. Since the banana width is in general much larger than the particle gyroradius, neoclassical transport theory predicts a larger magnitude of particle transport in the plasma than does classical transport.

Another effect of toroidal dynamics on plasma behavior, though not strictly transport, is the bootstrap current. Bootstrap current is a steady, self-induced toroidal current in the plasma resulting from radial neoclassical particle transport. The theoretical derivation of this phenomenon is far beyond the scope of this paper. However, its importance to a viable fusion tokamak is paramount, because a toroidal current is necessary in a tokamak to maintain plasma confinement and the boot-

strap current reduces the requirement for an external current drive. We are concerned with the bootstrap current in this thesis because the magnitude of this current may be susceptible to the temperature anisotropy that we are studying [6].

The final mechanism of particle transport theory is turbulent (or anomalous) transport. This refers to any transport attributable to mechanisms not already considered. These include perturbations to the idealized neoclassical model, such as variations in the electric and magnetic fields due to externally applied power fluctuations and internal plasma turbulence. In some circumstances the chracteristic step size of turbulent transport can be very large, meaning that turbulent particle transport can be significant. However, it can be controlled and minimized to an extent. In the work presented in this thesis, we simulate a plasma without turbulent transport. While this approach does not offer a complete view of plasma dynamics in the real system, it is sufficient to approximate a plasma in the irreducible transport limit.

1.3 National Spherical Torus Experiment

There are several variations on the standard design of a tokamak that are under investigation for viability as a fusion reactor. The variation in which we are interested in this thesis is the spherical tokamak. This design forms the plasma into a spherical torus—a small-aspect-ratio torus that is approximately a sphere with a hole through its center. The spherical tokamak offers a few advantages over other designs, but also faces some unique complications. It is unclear whether the spherical tokamak is better than other options as a fusion reactor, but its potential benefits make it worth studying. See [1] for a detailed description of the characteristics and properties, including potential advantages and disadvantages, of the spherical tokamak.

The National Spherical Torus Experiment (NSTX) is a major spherical tokamak project at Princeton Plasma Physics Laboratory (PPPL). A cutaway schematic is shown in Fig. 1.2. The

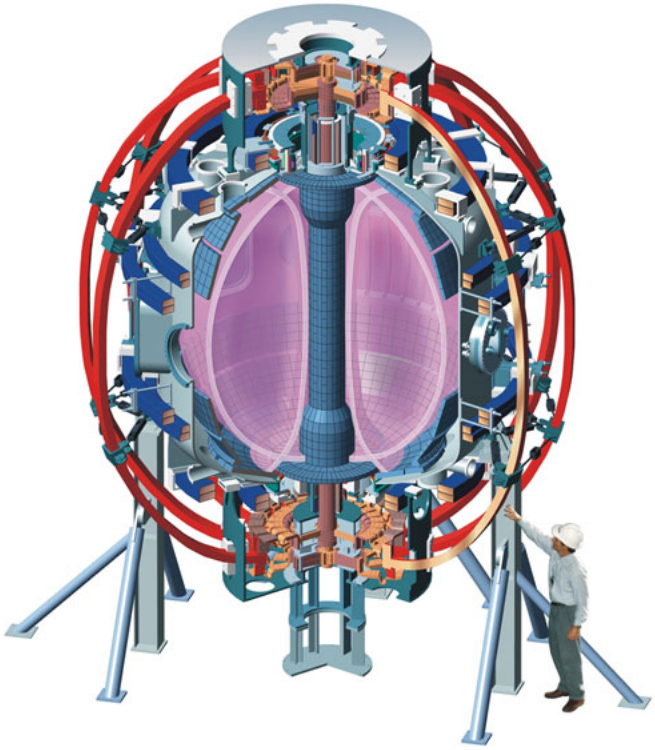

Figure 1.2 Cutaway view of NSTX. The spherical torus geometry is clear, as the plasma lies in a nearly spherical volume with only a thin column down the center. (Image courtesy of Princeton Plasma Physics Laboratory.)

goal of NSTX is to test the spherical tokamak concept in advanced regimes of plasma pressure, current, and other properties. Research on NSTX is valuable to the development of compact future tokamak designs that will allow for economic power generation [7].

The NSTX project has already resulted in a vastly improved knowledge of spherical tokamak physics [8]. Nevertheless, some information about NSTX plasmas cannot be obtained experimentally, due to lack of diagnostic tools. Fortunately, many of these details can be obtained by recourse to theoretical models. The focus of this thesis, temperature anisotropy, is one such quantity that is not experimentally diagnosable in NSTX. The study we present herein is based on computations according to toroidal dynamics, implying neoclassical transport. As mentioned in Section 1.2 our models are simplified to ignore potential turbulent effects. This is acceptable to observe the irreducible minimum of transport in NSTX. It is also reasonable because NSTX operates near the purely neoclassical transport levels [9].

1.4 Temperature Anisotropy

1.4.1 Definition

The temperature in a system is generally a measure of the average thermal kinetic energy of its constituents, which is determined by particle velocities. In highly collisional cases, the velocity distribution of a system is expected to be isotropic. In the case of a plasma under the influence of a magnetic field, however, the particles are constrained to gyrate about magnetic field lines but are unconstrained parallel to the field; furthermore, collisions may be infrequent. The plasma under these circumstances cannot necessarily be expected to have an isotropic velocity distribution. Thus in a magnetized plasma it is natural to define directional temperature values; that is, to determine average velocities based only on particles' average speed components in specific directions, and to scale these averages into corresponding temperatures. In this section we outline a standard

definition for directional temperature used in plasma physics [10].

In the case of the toroidal plasma of a tokamak, the direction parallel to the magnetic field lines is dominantly toroidal. It is along this direction that the guiding centers of gyrating particles ordinarily move most rapidly (See Appendix A for a summary of the motion of charged particles in a magnetic field). We denote the velocity of a particle in this direction as $v_{\|}$. The remainder of the particle velocity is directed in the plane orthogonal to the local magnetic field; the magnitude of this is denoted $v_{\perp}$. The parallel velocity $v_{\|}$ results from the free motion of particle guiding centers along the magnetic field lines, while $v_{\perp}$ is associated with particle gyromotion in the magnetic field as well as drift motion of the guiding centers. In the plane of the gyromotion, there is no preferential direction of motion; there is no need to decompose the velocity vector further because the velocity distribution in this plane is isotropic.

As discussed above, we can define parallel and perpendicular temperatures to correspond with $v_{\|}$ and $v_{\perp}$:

$$T_{\|} = \frac{m\langle v_{\|}^2 \rangle}{k}$$

and

$$T_{\perp} = \frac{m\langle v_{\perp}^2 \rangle}{2k},$$

where $\langle v_{\|}^2 \rangle$ and $\langle v_{\perp}^2 \rangle$ are mean-square values and k is the Boltzmann constant. There are a few items to note about these definitions. First, these temperatures are determined by particle mass and in a plasma, electrons and ions move independently. Thus these directional temperatures are species-dependent quantities. Indeed, this is true even for the total (nondirectional) temperature in plasmas and it is often the case that the electron temperature is not equal to the ion temperature, the one or the other being greater depending on methods of plasma heating. Second, it is customary in plasma physics to express temperatures in terms of energy per particle in eV rather than normal temperature units for computational ease; in such a case, k is omitted from the formulas above. Lastly, the formula for $T_{\perp}$ has an extra factor of 2 in its denominator when compared with $T_{\|}$. This

is because $T_\parallel$ is calculated using velocity components in a single dimension, while $T_\perp$ is determined by two dimensions of velocity components. In analogy with the dependence of standard temperature definitions on degrees of freedom, and so that $T_\parallel = T_\perp$ in an isotropic case, $T_\perp$ is given as an average per degree of freedom.

Finally, we are in a position to define temperature anisotropy. We measure temperature anisotropy with the quantity $T_\parallel/T_\perp$, so that if $T_\parallel/T_\perp = 1$ then $T_\parallel = T_\perp$ and the system is isotropic. On the other hand, $T_\parallel/T_\perp > 1$ or $T_\parallel/T_\perp < 1$ implies temperature anisotropy in the system. This definition is necessarily based on some set of particles over which the average values are computed. In our study we wish to characterize the spatial dependence of temperature anisotropy in NSTX, so we define temperature anisotropy at a point to be the value computed over all particles in a small neighborhood of that point.

1.4.2 Implications of Temperature Anisotropy

Prior to this study, the magnitude of temperature anisotropy in NSTX was unknown. It is possible to develop qualitative hypotheses about what to expect; for example, we expect $T_\parallel/T_\perp < 1$ on the inboard side of the torus due to the magnetic mirror effect, as discussed in Appendix A.3. However, the complexity of particle motion in a tokamak makes more precise guesses difficult. In this thesis we shall focus on ion temperature anisotropy. The results we present in this thesis by no means reflect electron temperature anisotropy in the plasma.

In consideration of the effects of anisotropy, studies suggest that the magnitude of the bootstrap current described in Section 1.2 is dependent on the ratio $T_\parallel/T_\perp$. If this ratio is greater than unity, the bootstrap current is expected to be enhanced from that predicted for an isotropic plasma. Furthermore, the flux of particles across flux surfaces increases with $T_\parallel/T_\perp$ [11, 12]. These results were not developed in the context of a spherical tokamak, but they suggest what we might expect from temperature anisotropy in NSTX. The enhanced bootstrap current may be positive news for

fusion power, since tokamaks require an internal plasma current for efficient and stable operation.

No current theoretical predictions regarding NSTX take anisotropy into account. Indeed, magnetohydrodynamic models assume isotropy [1]. This thesis seeks to determine to what degree the NSTX plasma is anisotropic; the results will serve to show to what extent an assumption of temperature isotropy is valid in NSTX.

1.4.3 Temperature Anisotropy and Collision Frequency

Beyond characterizing the ion temperature anisotropy, we also examine the dependence of temperature anisotropy on particle collision frequency in NSTX. As mentioned in Section 1.4.1, collisions tend to suppress anisotropy in the velocity distribution of the plasma. Thus, by increasing collision frequency, we expect temperature anisotropy features in the plasma to diminish in scale or to vanish. Some temperature anisotropy should be present as long as there are trapped particles in the tokamak, but these should be reduced as collisions increase. On the other hand, a decrease in collision frequency may enhance temperature anisotropy features or introduce features not observed more collisional cases.

Studying collisional dependence of temperature anisotropy allows us to make predictions about temperature anisotropy given changes in other plasma parameters. The ion-ion collision frequency in a plasma is proportional to $n/T^{3/2}$, where n is the plasma density and T is the total (nondirectional) temperature. Thus by observing temperature anisotropy at higher collision frequency, we can obtain some idea of how temperature anisotropy occurs at a lower temperature or at a greater density.

1.5 Thesis Overview

In this thesis we seek to determine the magnitude and spatial variation of temperature anisotropy in NSTX. The study is computational. We utilized the particle code GTC-NEO, a particle-in-cell (PIC) plasma code developed at PPPL, to simulate a plasma in NSTX. Our concern is with steady-state tokamak operation, so we computed temperature anisotropy for the plasma at neoclassical transport equilibrium. The anisotropy was computed along select spatial profiles and with several adjustments to collision frequency.

In Chapter 2, we describe the operation of GTC-NEO in greater detail. Sections 2.1–2.3 outline the underlying theory of the code, while Sections 2.4–2.5 cover the application of GTC-NEO to the problem of computing temperature anisotropy in NSTX. In Chapter 3, we present the results of the study. In Section 3.1 we present the radial and poloidal profiles of temperature anisotropy in NSTX at normal theoretical collision frequency. In Section 3.2 we present the same profiles as obtained for varied collision frequencies and observe the variation of temperature anisotropy features resulting from more or fewer collisions. We conclude with a discussion of the results obtained and future work in Sections 3.3-3.4.

Following the main text of the thesis we have included two appendices. Appendix A explains the motion of single particles subject to magnetic fields such as those found in a tokamak. Appendix B establishes coordinates and other customs of tokamak physics that may be unfamiliar to those outside of the field. Consult these appendices as needed to clarify terminology and concepts.

Chapter 2

Computing Temperature Anisotropy with GTC-NEO

2.1 The Drift Kinetic Equation

One tool of plasma modeling, the drift kinetic equation, forms the basis of the theory on which the particle code GTC-NEO operates. We present in this section a brief summary of the kinetic theory of plasmas, from which the drift kinetic equation arises. Kinetic theory is advantageous to plasma modeling because it produces very accurate models that encompass a variety of physical phenomena [1]. Our presentation will be neither lengthy nor rigorous; for a more complete treatment of kinetic theory, and in particular for a more rigorous development of the drift kinetic equation, see [5, 13].

Though it is sometimes possible to approximate a plasma as a continuous fluid, such an approximation is not valid when particle collisions are relatively infrequent, as is the case in high temperature magnetically confined plasma. A more accurate approach is to directly consider individual particle position and motion. On a macroscopic level, this is accomplished through the

velocity distribution function $f(\mathbf{r},\mathbf{v},t)$. The function f represents the statistical distribution of particles in both velocity space ($\mathbf{v}$) and configuration space ($\mathbf{r}$). Kinetic theory is concerned with the time evolution of f. This is determined by a kinetic equation of the form

$$\frac{\partial f}{\partial t} + \mathbf{v}\cdot\nabla f + \frac{\mathbf{F}}{m}\cdot\nabla_{\mathbf{v}} f = C[f]. \tag{2.1}$$

Here, $\mathbf{F}$ is the force acting on a specific particle, m is the particle mass, $\nabla_{\mathbf{v}}$ is the gradient in velocity space, and $C[f]$ is the collision operator, a situation-specific operator on f that represents the effect of particle collisions at each point in phase space. Since $\mathbf{F}/m$ represents the particle's acceleration, the left-hand side of Eq. (2.1) is simply the total time derivative of f, such that in the absence of collisions (that is, if $C[f]=0$), $\mathrm{d}f/\mathrm{d}t = 0$. Note that collisions can effect a change in f because they scatter particles away from a given phase space trajectory.

Now as described in Appendix A, individual particles in a plasma follow a trajectory that consists of gyromotion about a point known as a guiding center. The guiding center moves with velocity $v_{\parallel}$ parallel to the magnetic field lines, and undergoes motion perpendicular to the field known as drift, which in our case mostly results from neoclassical effects. In general, the gyroradius is small enough that the particle motion can be approximated accurately by the motion of the guiding center alone. This describes a much simpler trajectory. It is therefore preferable to use a kinetic equation in place of Eq. (2.1) in which the complexity of gyromotion is eliminated and f acts essentially as the velocity distribution not of particles themselves but of their guiding centers.

In fact, a more natural set of variables for a guiding center distribution is a phase space consisting of points $(\mathbf{R},\varepsilon,\mu,\vartheta)$ [5]. Here, $\mathbf{R}$ is the position of the guiding center, ε is the particle energy, μ is the magnetic moment of the particle due to its gyromotion, and ϑ is the gyrophase of the particle (see Appendix A for the definition of ϑ). Note that, for a particle with charge q and mass m in an electrostatic potential Φ and a magnetic field $\mathbf{B}$,

$$\varepsilon = \frac{mv^2}{2} + q\Phi(\mathbf{R},\mu,\vartheta), \tag{2.2}$$

where we have made the phase space dependence of Φ explicit, and

$$\mu = \frac{mv_\perp^2}{2B}. \tag{2.3}$$

Recall that $v_\perp$ is the velocity of the particle in the plane normal to $v_\parallel$; in this case, $v_\parallel$ is the velocity of the particle along magnetic field lines so $v_\perp$ mostly consists of velocity associated with particle gyromotion. Clearly, with the gyrophase information contained in ϑ, we have a phase space of independent variables that fully describe the particle's position and velocity. We shall demonstrate the benefit of this formulation.

The kinetic equation can be expressed with the new variables as

$$\frac{\partial f}{\partial t} + \dot{\mathbf{R}} \cdot \nabla f + \dot{\varepsilon}\frac{\partial f}{\partial \varepsilon} + \dot{\mu}\frac{\partial f}{\partial \mu} + \dot{\vartheta}\frac{\partial f}{\partial \vartheta} = C[f]. \tag{2.4}$$

From here we are prepared to introduce some useful simplifications to the model. First, μ is known to be an adiabatic invariant; that is, on relevant time scales, $\dot{\mu} \approx 0$. Second, we can time average the remaining terms in Eq. (2.4) over the gyromotion to obtain

$$\frac{\partial f}{\partial t} + \dot{\mathbf{R}} \cdot \nabla f + \bar{\dot{\varepsilon}}\frac{\partial f}{\partial \varepsilon} = \overline{C[f]}. \tag{2.5}$$

This is the drift kinetic equation. The barred quantities represent the gyroaveraged values. The drift kinetic equation is an effective tool for use in describing neoclassical transport and related effects. Indeed, at its core, GTC-NEO is designed to solve the drift kinetic equation globally with fields and geometry consistent with tokamak design.

2.2 The δf Method

Solving the drift kinetic equation may be no simple task. In this section and in the next we offer an outline of how GTC-NEO develops a solution to the drift-kinetic equation. This section focuses on the δf method, while the next explains how GTC-NEO utilizes the δf method to create a solution.

We can express the ion guiding center velocity distribution as

$$f = f_{SM} + \delta f \tag{2.6}$$

with f_{SM} being a shifted Maxwellian:

$$f_{SM} = n(r,\theta)\left(\frac{m}{2\pi T_0}\right)^{3/2} \exp\left\{-\frac{m}{T_0}\left[\frac{1}{2}\left(v_\parallel - U\right)^2 + \mu B\right]\right\}. \tag{2.7}$$

Here, T_0 is the ion temperature associated with the Maxwellian distribution, n is the spatial particle density, m is the particle mass, and U is the average particle speed in the direction of $\mathbf{B}$. The distribution δf is the deviation of f from a Maxwellian. The advantages of this simplification are discussed in [14, 15].

In this way we recast the problem of determining f as one of determining δf. While it may be the case that δf is not small compared with the total distribution f, the method is robust. The deviation δf need not be small; as long as it is not larger than f, the approach is valid [15]. The code GTC-NEO utilizes the δf approach.

A peculiarity of the δf method as developed for GTC-NEO is in the way the code produces the directional temperature values in which we are interested. Whereas we seek the values $T_\parallel$ and $T_\perp$ as absolute quantities, GTC-NEO produces the relative values $\Delta T_\parallel = T_\parallel - T_0$ and $\Delta T_\perp = T_\perp - T_0$. These values are the deviation of the directional temperatures from the Maxwellian temperature T_0, just as δf is the deviation of f from f_{SM}. Thus to translate from the relative values to the anisotropy ratio that we seek, we use the formula

$$\frac{T_\parallel}{T_\perp} = \frac{\Delta T_\parallel / T_0 + 1}{\Delta T_\perp / T_0 + 1}. \tag{2.8}$$

2.3 Computing δf with GTC-NEO

In this section we explain the algorithm by which GTC-NEO computes δf. The code initializes a large number of simulation particles according to user-specified initial conditions and tracking their

motion in phase space. It is shown in [14,15] that if the simulation particle number is large enough, then the simulation particles' discrete distribution is approximately the same as the continuous distribution δf. The evolution of δf is rigorously tied to the evolution of individual simulation particle coordinates in phase space. The problem of computing δf is now simply to track the motion of those particles.

The code is a PIC simulation, meaning that it iteratively evolves particle positions over small time steps. Particles are simulated in a three-dimensional toroidal geometry with a built-in mesh. At the vertices of the PIC mesh the electric and magnetic fields are calculated each time step based on particle position and motion as well as on exterior fields. With the fields thus calculated, they can be determined at a particle's position by interpolating the values from the vertices. Given that information, GTC-NEO uses a Runge-Kutta solver to evolve particle position. Naturally, GTC-NEO does not exclude particle collisions. Coulomb collisions between particles are simulated by a Monte Carlo method that changes particle velocity but conserves momentum and energy. Collisions are relatively infrequent in the plasma being studied, so the characteristic time scaling used in the code for collisions is adjusted appropriately from that used for particle position and velocity evolution.

We have stated that the algorithm requires that the code be initialized with the initial value of δf. Thus GTC-NEO runs from initial conditions obtained from experiment. In fact, the simulations discussed in this thesis are based on data obtained from experiments performed at NSTX. The code reads in data on particle density and temperature and initializes simulation particles with corresponding positions and velocities such that the simulation particle distribution roughly matches the input data. From this initial distribution, GTC-NEO runs for a user-specified duration to observe large-scale evolution of the plasma to neoclassical equilibrium. The total wall time necessary to obtain the specified simulation duration is dependent on parameters given by the user; we shall discuss this further in Section 2.5.

As is the case with most modern large scale codes, GTC-NEO is a parallel code. The user specifies the number of processes to utilize, and each simulates a portion of the total number of simulation particles. Quantities that require information from all processes, like electric and magnetic field values and the directional temperatures in which we are interested, are computed using the Message Passing Interface parallel processing standard.

2.4 Computing Temperature Anisotropy

As we have previously mentioned, we are interested in temperature anisotropy in NSTX as the device operates at steady state. We diagnose steady state by observing energy flux through flux surfaces throughout the plasma. Indeed, as described in Section 2.3, GTC-NEO is designed to simulate the plasma until it reaches such a steady state. The simulation divides the torus into radial shells, which are themselves toroidal surfaces, through which GTC-NEO measures and records total energy flux each time step. With these data it is possible to observe the point in time at which flux equilibrium is achieved and thus to identify the time after which temperature anisotropy measurements are valid. As an example, see Fig. 2.1. Observe that the energy flux becomes flat very shortly after the simulation begins, meaning that equilibrium is achieved and we can observe temperature anisotropy. We expect this, because the experimental data from NSTX that initialize the code should reflect the tokamak approximately at steady state. The initial disturbances in Fig. 2.1 most likely reflect the settling out of noise introduced by initializing the simulation particles.

The computation of temperature anisotropy using GTC-NEO is very simple. Since it is a PIC code, GTC-NEO tracks the velocity components of each simulation particle. Due to the code structure, it is a straightforward matter to isolate $v_{\|}$ and $v_{\perp}$ for each particle. As such, it is possible to average $v_{\|}^2$ and $v_{\perp}^2$ over all simulation particles within a region, which yields (see Sections 1.4.1

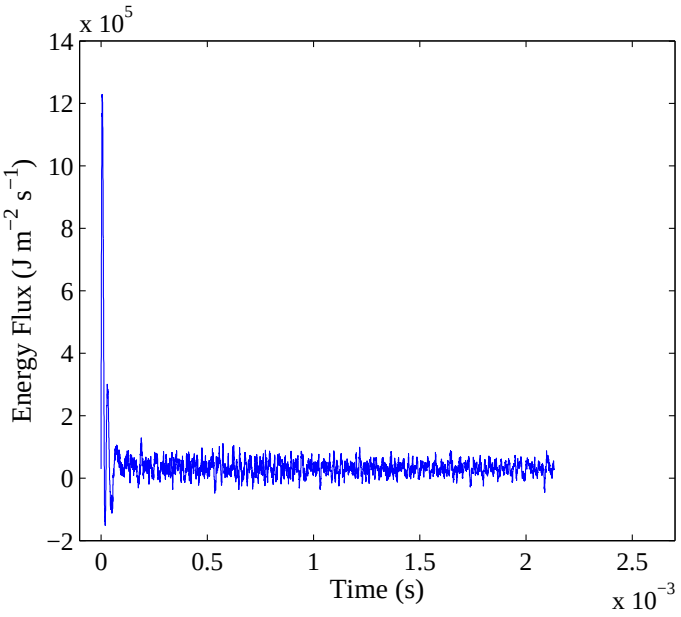

Figure 2.1 Time dependence of energy flux through a given flux surface. In this case, the surface in question is $r = 0.5$. Observe that the system quickly settles into a steady state of energy flux; though it shows noise, it is flat enough for our purposes.

and 2.2) the respective directional temperature values $\Delta T_{\|}$ and $\Delta T_{\perp}$. The region chosen is a small volume centered at a point that is chosen by the user; in its form as used for this thesis, GTC-NEO accepts 45 simultaneous locations to compute directional temperatures in a single run. Our anisotropy calculation for each point for a single time step is simply the quotient in Eq. (2.8).

Over very small time scales, near the order of the simulation time step, $T_{\|}$ and $T_{\perp}$ fluctuate, as is to be expected from quantities in a particle simulation. Hence it is necessary to time average $T_{\|}/T_{\perp}$ over the duration identified in our appeal to the energy flux time profile. Over sufficiently long timescales, the temperature values steadily decrease as a result of the total loss of energy of the system to the environment; though energy flux is steady, it is nonzero. However, the quotient $T_{\|}/T_{\perp}$ remains reasonably constant over time, apart from short scale fluctuations (See Fig. 2.2). Thus the time average is valid for our purposes. Indeed, we averaged anisotropy over two different time intervals and detected no significant change in the resulting spatial profiles.

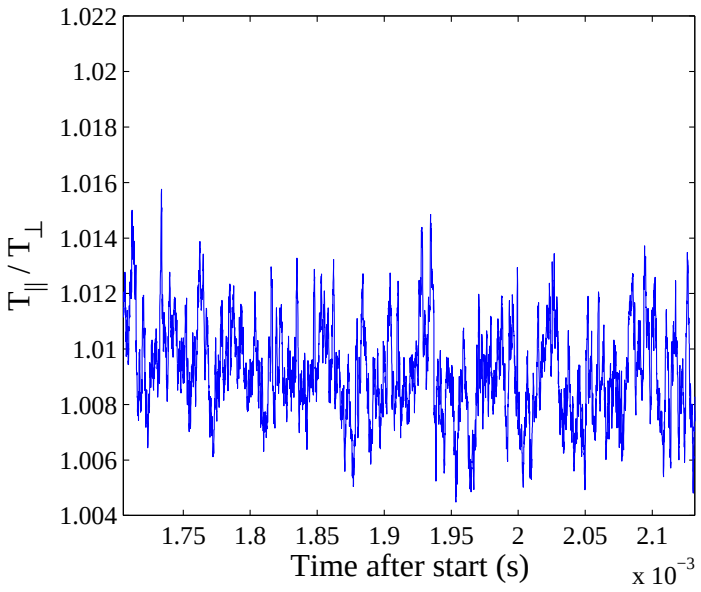

Figure 2.2 Time dependence of $T_{\|}/T_{\perp}$ over a selected interval. These data represent the temperatures in one single location in the simulation. The profile is noisy and some long-scale variation may occur, but it is flat enough that we can obtain a time average.

The process can thus be summarized as follows: Using data exported from a run of GTC-NEO, we select a time interval over which energy flux is constant, compute $T_{\|}/T_{\perp}$ for each time step at each specified location, and average $T_{\|}/T_{\perp}$ over the time interval. Doing so at judiciously chosen points in the tokamak yields poloidal and radial profiles of $T_{\|}/T_{\perp}$. We repeat the process for each collision frequency that we investigate.

2.5 Specifics of GTC-NEO Runs and Diagnostics

One of the goals of this thesis is to observe how the temperature anisotropy varies as a function of position in the torus. This knowledge allows us to understand better the causes of anisotropy; we can compare spatial trends with those in other location-dependent quantities to observe whether they are correlated. Thus, while other studies of anisotropy consider a flux-surface averaged $T_{\|}/T_{\perp}$ [6,11,12,16], we calculate the quantity locally at various points on the toroidal cross-section

of the tokamak, as described in Section 2.4.

In this section we explain the specific details of our runs of GTC-NEO. See Appendix B for an explanation of toroidal coordinates used here and in the next chapter. We chose three radial locations along which to compute a poloidal profile and three poloidal locations along which to compute a radial profile. The poloidal profiles were computed at $r = 0.1$, $r = 0.5$, and $r = 0.9$ (the radial coordinate r is given as a fraction of the plasma radius, so that $r = 1$ refers to the plasma edge), giving a view of anisotropy near the plasma axis, halfway from the axis to the plasma edge, and near the edge of the plasma. We computed radial profiles at $\theta = 0$, $\theta = \pi/2$, and $\theta = \pi$, giving a view of anisotropy through the weak, intermediate, and strong magnetic field regions, respectively. Since dynamics in the tokamak are independent of the toroidal coordinate ζ, the "points" we have selected actually extend as circles around the torus; the radial and poloidal coordinates are identified, but we consider points with any value of ζ.

The radial profiles offer particularly useful data as each passes through a different regime of particle trapping. All particles lying in a banana orbit ought to pass through the $\theta = 0$ line periodically, whereas only some will pass through the $\theta = \pi/2$ line and none reach $\theta = \pi$. Thus the profiles chosen should deliver a clear view of what anisotropy trends can be associated with particle trapping. Furthermore, in general, the trend is expected to be that $T_{\|}/T_{\perp}$ decreases for all particles as θ increases from 0 to π. This is a result of the fact that $v_{\|}$ should decrease along a magnetic field of increasing magnitude, as described in Appendix A.3.

Along the lines described, we sampled at uniform intervals. The points at which we sampled are listed in Fig. 2.3. The resulting profiles are presented in Section 3.1. We obtained our results running GTC-NEO on 48 processors with 320 000 simulation particles per precessor. This is a fairly small run; GTC-NEO is capable of much larger scale computation, but the given run parameters were sufficient for this anisotropy study. A larger run, however, might produce smoother data. Each run with the given parameters lasted approximately 75 hours.

Profile Sampling Locations

θ	0	$\pi/8$	$\pi/4$	$3\pi/8$	$\pi/2$	$5\pi/8$	$3\pi/4$	$7\pi/8$	π
r	0.1	0.2	0.3	0.4	0.5	0.6	0.7	0.8	0.9

Figure 2.3 Values of θ (r) at which the poloidal (radial) anisotropy profiles were sampled.

Another goal of this thesis is to observe the dependence of temperature anisotropy on collision frequency. As we discussed in Section 1.4.3, if ν is the ion-ion collision frequency, then $\nu \propto n/T^{3/2}$. While it is not possible to vary ν without varying either n or T in a real plasma, GTC-NEO allows ν to vary independently of either. This does not necessarily determine a physically permissible system, but it does permit us to observe the effect of ν on temperature anisotropy. From these observations we can make predictions about the behavior of temperature anisotropy in plasmas in which T and n dictate a larger or smaller value of ν. We gave some predictions regarding collisional dependence of temperature anisotropy in Section 1.4.3.

Let ν_0 be the theoretical expected collision frequency; in the case of our runs with NSTX, this was approximately $\nu_0 = 1.4 \times 10^4$ Hz. We repeated the run of GTC-NEO described above for the collision frequency $\nu_0/100$, $\nu_0/10$, $10\nu_0$, and $100\nu_0$. The results are described in Section 3.2.

Chapter 3

Results: Profiles and Collision Frequency Dependence

3.1 Anisotropy Profiles

In the case of collision frequency ν_0, we obtained profiles of $T_\parallel/T_\perp$ at the locations listed in Section 2.5. The radial profiles are shown in Fig. 3.1(a) and the poloidal profiles are shown in Fig. 3.1(b). Evidently, anisotropy is present at several points along the line, but never large. The variation between $T_\parallel$ and $T_\perp$ never exceeds 5%.

Two items in particular are worthy of comment in Fig. 3.1. First, note in Fig. 3.1(a) the peak at around $r = 0.8$ in the $\theta = 0$ profile. That location is a region in which many particles trapped in a banana orbit should pass. It is odd that the peak should appear there; if anything, we should expect the opposite. Since $v_\perp$ generally exceeds $v_\parallel$ for a trapped particle, we expect that a trough should appear where we have observed a peak. We hasten to state that the peak is in the region in which we would expect the greatest value of $v_\parallel$ for trapped particles, and other more complex dynamics could be at play to cause the spike seen (especially since trapped particles should occur in equal or

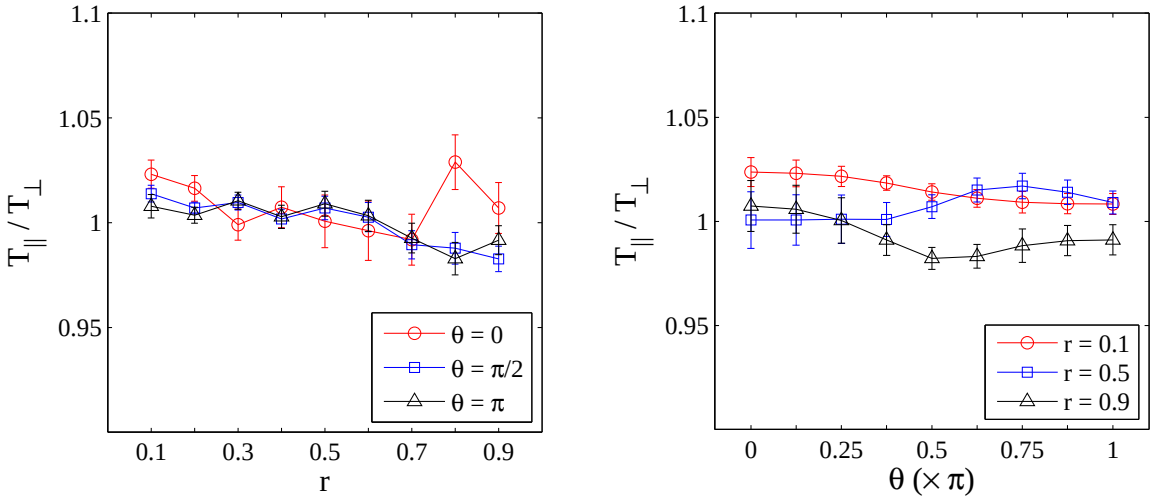

(a) **(b)**

Figure 3.1 Ion temperature anisotropy profiles along lines of (a) constant θ and (b) constant r. Note that r is normalized, so $r = 0$ refers to the plasma axis while $r = 1$ refers to the outer edge of the plasma. The error bars represent $\pm 3\sigma$. While some variation is evident, $T_\parallel / T_\perp$ always remains near unity.

greater quantities at $r = 0.9$, being nearer the edge of the plasma). The second noteworthy item is in Fig. 3.1(b). In the $r = 0.5$ profile, $T_\parallel / T_\perp$ increases as θ increases, contrary to our expectation. In both cases, the variations in our work from $T_\parallel / T_\perp = 1$ remained small.

Little work has been done to ascertain the effect of temperature anisotropy in a spherical tokamak. For a large-aspect-ratio tokamak, it is predicted that temperature anisotropy will substantially increase bootstrap current from the prediction based on an isotropic plasma [6]. Likewise, the radial energy and particle flux is expected to increase [11, 12]. However, these predictions may be qualitatively applied to the small aspect ratio of a spherical tokamak only with care. Furthermore, the increases expected in those studies depend on the assumption of a flux surface average of $T_\parallel / T_\perp$ not near 1. This is certainly not the case, as we have observed, in NSTX. Thus there is little evidence from which to draw conclusions regarding the effect of the observed anisotropy in this study, but the fact that $T_\parallel / T_\perp$ remains near unity suggests that assumptions of isotropy in

theoretical work, as described in Section 1.4.2, on NSTX are valid.

3.2 Dependence on Collision Frequency

As described in Section 2.5, we used GTC-NEO to simulate the plasma with varying values of ν to observe how $T_\parallel/T_\perp$ depends on collision frequency. The results are shown in Fig. 3.2. We failed to obtain useful data at $\nu = 100\nu_0$. At that collision frequency, the code never settled into the energy flux equilibrium necessary to examine a steady state plasma. The most likely explanation for this is that since GTC-NEO is a code based on the drift kinetic equation, it becomes inaccurate when particle collisions become frequent and the plasma leaves the collisional realm described by kinetic theory. Based on this assumption, the data from the $\nu = 10\nu_0$ case should be considered suspect, though we did obtain energy flux equilibrium from that run.

Most notable from the figures are the substantial peaks in Figs. 3.2(b) and 3.2(d), like the one observed in Section 3.1. Observe that these peaks are most prominent for $\nu = \nu_0/100$ and that they vanish for $\nu = 10\nu_0$. This supports our expectation that the magnitude of anisotropy features should vary inversely with collision frequency. It also suggests that the feature noticed in Fig 3.1(a) may not be an artifact of computation but a real feature in the simulated plasma. That the peaks are larger for $\theta = 0$ than for $\theta = \pi/2$ and nonexistent at $\theta = \pi$ supports our previous guess that the location of the peaks corresponds with the location of trapped particles in a banana orbit. Somehow it seems that trapped particles uninhibited by collisions contribute relatively heavily to an increase in $T_\parallel/T_\perp$. As expected, collisions act to suppress anisotropy and isotropically distribute energy.

Even for the smallest collision frequency, $T_\parallel/T_\perp$ still remains near unity. At only one point does it deviate by more than 5%. Other potentially interesting features occur in the profiles: in particular, the visible variation between profiles of various collision frequencies at $r = 0.9$ at both $\theta = 0$ and $\theta = \pi$. However, these features are small and may serve little purpose to understanding the overall

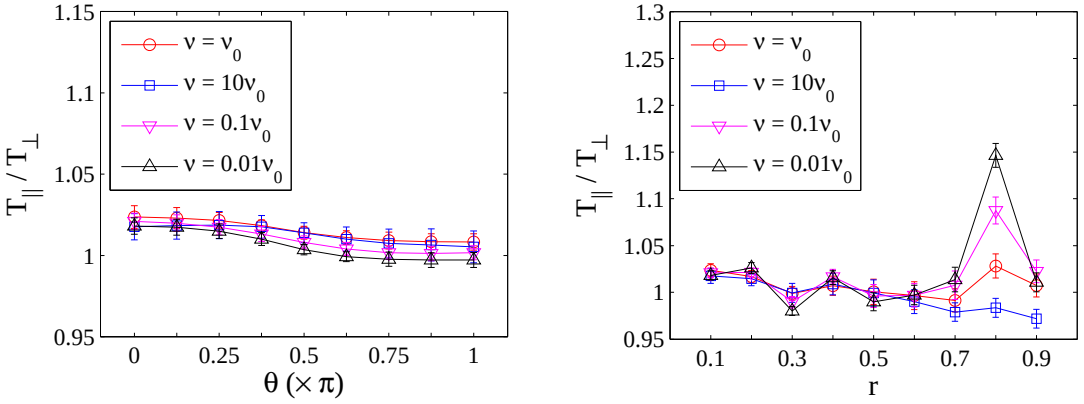

(a) $r = 0.1$

(b) $\theta = 0$

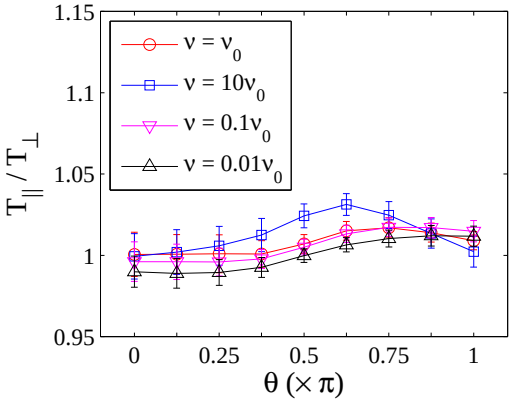

(c) $r = 0.5$

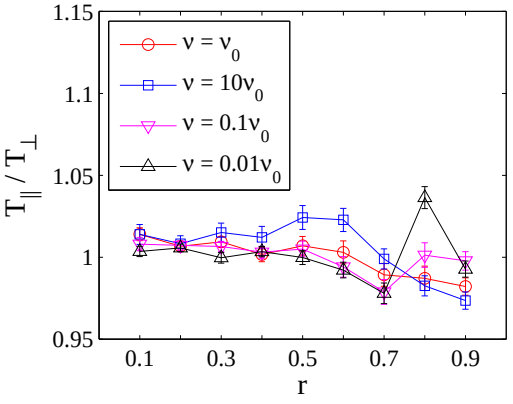

(d) $\theta = \pi/2$

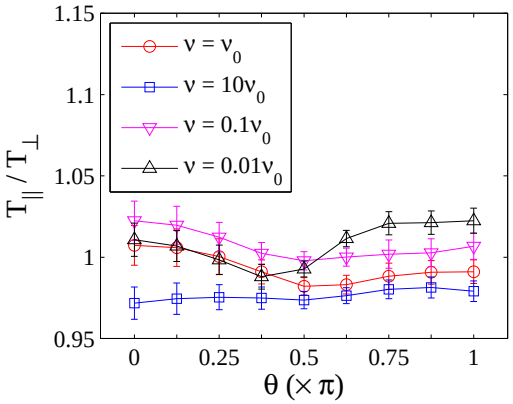

(e) $r = 0.9$

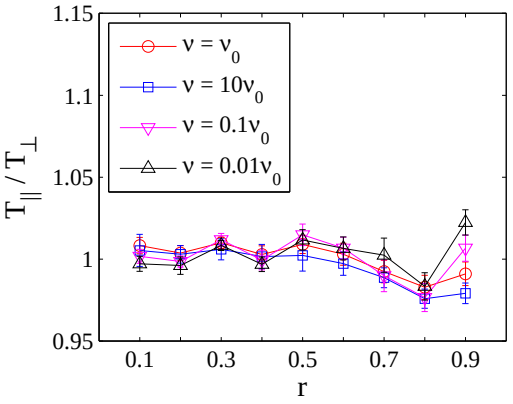

(f) $\theta = \pi$

Figure 3.2 Comparison of each profile from Fig. 3.1 with various collision frequencies ν. The error bars, as before, represent $\pm 3\sigma$. The value ν_0 is the theoretical collision frequency and the one used in Fig. 3.1. Note the substantial peak of $T_\parallel/T_\perp$ in (b) and (d). Also, observe that (b) has a different vertical scale than do the other plots.

physics in NSTX. Other theoretical studies are necessary if we wish to determine whether that is the case.

3.3 Future Work

We have already noted several features in the temperature anisotropy profiles that fail to align with our predictions. In particular, the large spike in $T_\parallel/T_\perp$ on the radial profiles at $r = 0.8$, as well as the failure of some of the poloidal profiles to decrease with increasing θ, demand further attention. A first step in understanding both of these phenomena would be to produce finer poloidal and radial resolution of the profiles; it would be illuminating to see, for example, how the spike at $r = 0.8$ changes with θ and how the profile varies from $r = 0.7$ to $r = 0.9$. Nevertheless, an understanding of the causes of the features may only arise by recourse to theory independent of computation with GTC-NEO.

Perhaps more important than understanding those features, however, is understanding the overall effects of the temperature anisotropy. We have conjectured repeatedly regarding whether the levels of temperature anisotropy in NSTX are large enough to challenge the predictions of theory that assumes isotropy. At the magnitudes of $T_\parallel/T_\perp$ observed, which remain within 5% of unity, we do not expect significant deviations from the isotropy assumptions of existing theory. Nevertheless, these conjectures are without strong basis, because there is minimal prior work studying the effects of temperature anisotropy in a spherical tokamak. It would be prudent to develop studies similar to those described in [6, 11, 12], but designed with a spherical tokamak in mind. These studies would serve to determine whether small deviations of temperature anisotropy from unity have a noticeable effect to alter predictions of magnetohydrodynamic equilibrium theory.

Finally, this study focused specifically on geometry and initial conditions unique to NSTX. It is unclear whether any of the results may be generalized. To ascertain whether we may generalize

the results to all spherical tokamaks, or to tokamaks in general, it is necessary to conduct the same study on a variety of tokamak designs. In fact, performing the study on a large-aspect-ratio tokamak will allow better cross-referencing with the studies in [6, 11, 12].

3.4 Conclusion

We used the PIC code GTC-NEO to evaluate the level of temperature anisotropy in NSTX and to produce profiles of local temperature anisotropy. In the case of normal, i.e., physically expected collision frequency, anisotropy varies up to 5%, with a small but clear peak at $r = 0.8$ that does not agree with our predictions. We obtained data for three other collision frequencies as well, from which we observed that the same peak was significantly greater at smaller collision frequency, implying that collisions play a strong role in suppressing anisotropy. This is consistent with our previous expectations. It is noteworthy, however, that away from trapping regions, anisotropy varied little if at all with collision frequency, and not in accordance with our expectations that collisions would suppress anisotropy.

Our results can thus be summarized: spatial profiles of temperature anisotropy in NSTX display complex features that in some cases seem to contradict predictions of toroidal dynamics, but they remain near unity. It is likely that these findings do not affect the existing theory discussed in Section 1.4.2, but this cannot be confirmed without further study. It may be the case that magnetohydrodynamic equilibrium is upset by even such modest levels of anisotropy, because, in the equilibrium state, pressure and temperature are functions of the flux surface only [1]. Then again, there may be no significant change to existing theory due to these findings. Hence the implications of our results are somewhat inconclusive; however, we have accomplished our goal to compute temperature anisotropy in NSTX. Our findings will be useful to related future studies as they pursue this problem further.

Appendix A

Particle Motion in a Magnetic Field

To understand the dynamics of a magnetized plasma, one must have a knowledge of single particle behavior under the influence of a magnetic field. In this appendix we present an overview of relevant characteristics of particle motion. In the case of uniform magnetic field and no electric field, we shall show the derivation based on Newtonian mechanics; for more complex field configurations, we shall present the result without proof or simply give a qualitative explanation, as necessary to the understanding of this thesis. See [10] for additional information.

A.1 Gyromotion: Uniform Magnetic Field

Suppose a particle with charge q and mass m moves with velocity $\mathbf{v}$ in a constant magnetic field $\mathbf{B}$. The magnetic force on the particle is $\mathbf{F}_B = q\mathbf{v} \times \mathbf{B}$. According to Newton's second law, then,

$$m\dot{\mathbf{v}} = \mathbf{F}_B = q\mathbf{v} \times \mathbf{B}. \tag{A.1}$$

Without loss of generality, we can assume $\mathbf{B}$ is in the z direction, i.e., $\mathbf{B} = B\hat{\mathbf{z}}$. Then Eq. (A.1) yields a coupled system of first order equations:

$$\dot{v}_x = (qB/m)\, v_y \tag{A.2}$$

$$\dot{v}_y = -(qB/m)\, v_x \tag{A.3}$$

$$\dot{v}_z = 0. \tag{A.4}$$

The solution to Eq. (A.4) is trivial:

$$v_z = v_{z0}, \tag{A.5}$$

where v_{z0} is the initial velocity in the z direction. Differentiating Eq. (A.2) with respect to time and substituting Eq. (A.3), we obtain the second order equation

$$\ddot{v}_x = -(qB/m)^2 v_x. \tag{A.6}$$

If we define the cyclotron frequency $\omega_c = |q|\, B/m$, the solution to Eq. (A.6) is

$$v_x = A_1 \cos \omega_c t + A_2 \sin \omega_c t,$$

where A_1 and A_2 are constants of integration. For mathematical convenience, we express this as the real part of a complex exponential function:

$$v_x = v_\perp e^{i(\omega_c t + \delta)}, \tag{A.7}$$

where $\delta = \arctan(-A_2/A_1)$ and $v_\perp = \sqrt{A_1^2 + A_2^2}$ is the maximum value that v_x reaches, and happens to be the magnitude of the particle's velocity perpendicular to $\mathbf{B}$. We can now substitute Eq. (A.7) back into Eq (A.2) to obtain

$$v_y = \pm i v_\perp e^{i(\omega_c t + \delta)}. \tag{A.8}$$

Here the $\pm$ indicates the sign of q, since ω_c was defined with $|q|$. Note from the factor of i that v_x and v_y are out of phase by $\pi/2$. Thus the equations for v_x and v_y describe circular motion with

frequency ω_c in the plane perpendicular to **B**. For simplicity, we choose the x and y axes such that $\delta = 0$. This is equivalent to choosing axes such that the initial velocity is entirely in the xz plane.

We can now integrate Eqs. (A.7), (A.8), and (A.5) to obtain the time dependent position of the particle (taking the real parts to express the physical values):

$$x = x_0 + \frac{v_\perp}{\omega_c} \sin \omega_c t \tag{A.9}$$

$$y = \left(y_0 \mp \frac{v_\perp}{\omega_c} \right) \pm \frac{v_\perp}{\omega_c} \cos \omega_c t \tag{A.10}$$

$$z = z_0 + v_{z0} t, \tag{A.11}$$

where x_0, y_0, and z_0 are the initial position coordinates of the particle. Clearly, the particle moves in a circular orbit in the plane normal to **B** around the point $(x_0, y_0 \mp (v_\perp/\omega_c), z)$. This point is known as the guiding center of the particle and moves with constant velocity $\mathbf{v}_{gc} = v_\parallel \hat{\mathbf{z}}$, the subscript implying that the guiding center moves parallel to the magnetic field. Of course, $v_\parallel = v_{z0}$. Hence the particle follows a helical trajectory around a magnetic field line; in the special case of $v_{z0} = 0$, the guiding center is stationary and the particle's trajectory is a circle. The value $v_\perp/\omega_c$ is known as the gyroradius and is the radius of the circular trajectory. The value $\vartheta = \omega_c t$ is the gyrophase, tracking the phase of the particle's gyromotion.

A.2 Guiding Center Drift Motion

In Section A.1 we derived the simplest case of particle motion in a magnetic field. In that situation, the particle was found to gyrate in a circular orbit about a guiding center that remains centered on a single magnetic field line. In more complicated configurations, such as the presence of a nonzero electric field or variations in magnetic field strength, other influences act to cause the guiding center to move from one magnetic field line to another. This motion is known as drift. We present some principle examples of drift motion without derivation.

A.2.1 Uniform Electric Field and E × B Drift

Suppose, in addition to the magnetic field, we introduce a uniform electric field **E**, so that the particle undergoes force according to the Lorenz force law: $\mathbf{F} = q(\mathbf{E} + \mathbf{v} \times \mathbf{B})$. In this and all following descriptions of drift motion, the particle still gyrates about a guiding center. The trajectory of the guiding center, however, changes. In this case, the guiding center now moves with velocity

$$\mathbf{v}_{gc} = v_{\parallel}\hat{\mathbf{z}} + (\mathbf{E} \times \mathbf{B})/B^2. \tag{A.12}$$

Clearly, as long as **E** is not parallel to **B**, then $(\mathbf{E} \times \mathbf{B}) \perp \mathbf{B}$ so $\mathbf{v}_{gc}$ has a perpendicular component. The guiding center drifts perpendicular to the field with velocity of magnitude $(E/B)\sin\varphi$, where φ is the angle between **E** and **B**. This is commonly called **E** × **B** drift. Note that when B is large, as in the case of a magnetized tokamak plasma, the **E** × **B** drift is small regardless of φ.

It is noteworthy that this effect is actually not limited to forces due to an electric field. There is an analog to the **E** × **B** drift whenever the particle moves through another force field **F** not parallel to **B**, such as gravity. The general form of the adjustment to $\mathbf{v}_{gc}$ is

$$\mathbf{v}_F = (\mathbf{F} \times \mathbf{B})/qB^2. \tag{A.13}$$

We shall revisit Eq. (A.13) in Appendix A.2.3.

A.2.2 Perpendicular Magnetic Field Gradient and ∇B Drift

Consider again the original field **B** in the z direction, but now suppose that its magnitude B varies in a direction perpendicular to **B**. We assume that the gradient scale of B is large compared with the particle gyroradius $v_{\perp}/\omega_c$, or in other words, that the spatial variation of B along the gradient is small. Gyromotion causes the particle to move between regions of greater and lesser field strength, meaning that the gyroradius is not constant through a full period of revolution. The net effect is a drift perpendicular both to the gradient and to the field, known as ∇B drift. Mathematically, the

adjustment to $\mathbf{v}_{gc}$ due to this effect is

$$\mathbf{v}_{grad} = \frac{W_\perp}{q}\frac{\mathbf{B}\times\nabla B}{B^3}, \tag{A.14}$$

where $W_\perp$ is the particle kinetic energy resulting from $v_\perp$.

A.2.3 Curved Magnetic Field Lines and Curvature Drift

Now consider a magnetic field $\mathbf{B}$ such that the cross-field magnitude gradient is zero but with curved field lines. Again, the curvature length scale, and thus the local radius of curvature, must be large compared to the gyroradius. If we consider a particle moving along a field line instantaneously and transform to the rotating frame of reference in which the particle's trajectory is straight, then the particle's motion is along a "straight" field line, but the particle is under the influence of a centrifugal force given by

$$\mathbf{F}_{cf} = mv_\parallel^2\mathbf{R}_c/R_c^2. \tag{A.15}$$

Returning to the note at the end of Section A.2.1, we can substitute Eq. (A.15) into Eq. (A.13) to determine the approximate drift due to magnetic field curvature:

$$\mathbf{v}_{curv} = \frac{mv_\parallel^2}{qB^2}\frac{\mathbf{R}_c\times\mathbf{B}}{R_c^2}. \tag{A.16}$$

A.3 Invariance of Magnetic Moment and Magnetic Mirrors

So far we have considered effects of the magnetic field that cause particle motion perpendicular to the field. Now we shall examine one important effect that influences particle motion parallel to the field. We must first, however, discuss the particle magnetic moment, μ, resulting from gyromotion.

The value of μ is determined by $v_\perp$ as shown in Eq. (2.3). It is also the case that μ is invariant on the time scales with which we are concerned, as proven in [10].

Now, consider a magnetic field in which ∇B is parallel to $\mathbf{B}$. Suppose a particle moves with guiding center velocity in the direction of ∇B. This means that B increases along the particle's trajectory. As a result, $v_\perp$ must also increase to maintain μ. Of course, the increase in $v_\perp$ must be accompanied by a corresponding decrease in $v_\parallel$ by conservation of energy. Mathematically, we have $\mu B = mv_\perp^2/2 = W_\perp$, so if W is the particle's total kinetic energy, then

$$mv_\parallel^2/2 = W - \mu B. \tag{A.17}$$

Hence if B increases to the point at which $\mu B = W$, then $v_\parallel = 0$ and all of the particle's motion must be in the perpendicular direction. Qualitatively, the guiding center slows and the particle velocity associated with gyromotion increases as B increases, until the particle reaches the limit at which $v_\parallel = 0$ and is reflected in the opposite direction. This is known as the magnetic mirror effect and occurs in tokamaks, as described in Section 1.2. This does not occur for all particles in a given field; clearly, from Eq. (A.17), for a particle to undergo reflection in a field with maximum magnitude B_{max}, the particle must have $\mu > W/B_{max}$. For a particle with $\mu < W/B_{max}$, $v_\parallel$ will never reach zero, but will decrease to a minimum.

Appendix B

Toroidal Coordinates and Conventions for Tokamak Plasmas

B.1 Toroidal Coordinates

When specifying position in a torus, Cartesian coordinates and other commonly used systems can be awkward and cumbersome. However, the unique symmetry of the torus lends itself to a special coordinate system. Inasmuch as the torus is a cylinder curved around into itself, it is natural to use a coordinate system adapted from canonical cylidrical coordinates. Rather than offer formulae for the coordinate transformation from other systems, which would be cumbersome and unenlightening, we explain the system according to its analogs with a cylindrical coordinate system.

In cylindrical coordinates, z determines a plane in which r and θ then act as polar coordinates centered on the z axis. Analogously in cylindrical coordinates, ζ determines a cross-section of the torus, in which r and θ then act as polar coordinates centered on the toroidal axis. See Fig. B.1 for a visualization of this system. It is worth noting that, while z in cylindrical coordinates represents

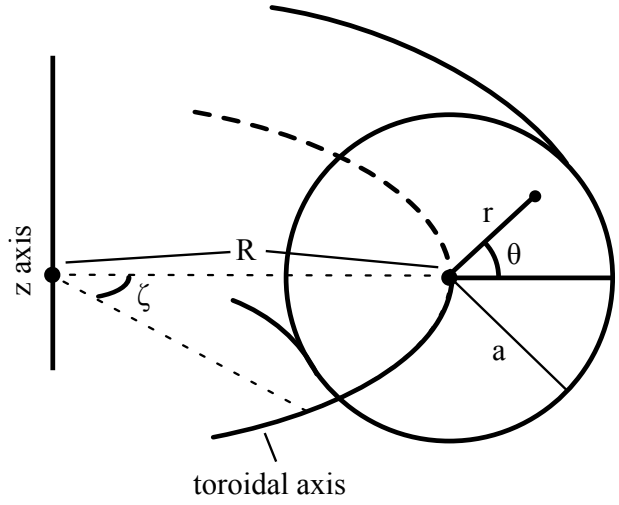

Figure B.1 Toroidal coordinate system. In any toroidal cross-section, the variables r and θ act as polar coordinates with origin on the toroidal axis. The variable ζ determines the cross-section. The values R and a are the major and minor radii, respectively. The z axis is included as the symmetry axis of the torus.

length, ζ in toroidal coordinates represents an angle, the natural choice due to the circular nature of the torus. We call r the radial coordinate, while θ is the poloidal coordinate and ζ is the toroidal coordinate.

In a mathematical sense, r can be arbitrarily large (though not with a one-to-one correspondence between points and coordinate triplets). However, when considering a physical torus with finite minor radius a, it is usually sufficient to consider $r < a$. As such, it is customary to represent r in normalized units, so that $r = 0$ refers to the toroidal axis, $r = 1/2$ represents $r = a/2$, and $r = 1$ is the plasma edge. In fact, this representation of r is particularly useful in the case of tokamak plasmas, because in general they do not actually have circular toroidal cross-sections, as is evident in the case of NSTX (Fig. 1.2). The radial coordinate for a tokamak plasma no longer represents a constant distance to the edge of the plasma independent of θ, but refers to a specific magnetic flux surface. Refer to Section B.2 for a brief explanation of flux surfaces. Now for a given θ, the value of r between 0 and 1 represents the fractional distance to the last closed flux surface of the plasma, and for different values of θ, a given r always refers to the same flux surface (see Fig. B.2).

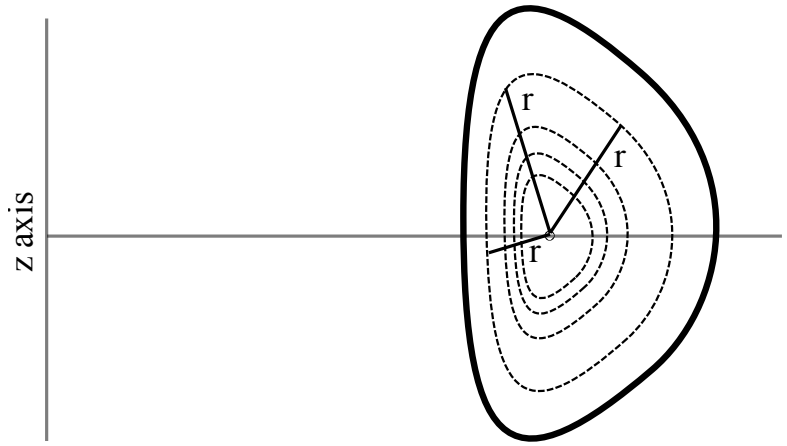

Figure B.2 Approximate cross-section of a tokamak plasma. The concentric dashed shapes are example flux surfaces. The radial coordinate r is constant as shown on the dotted surface, despite the irregular shape.

B.2 Flux Surfaces and Tokamak Conventions

We discuss flux surfaces and several other concepts specific to tokamaks in various sections throughout the main body of this paper. In this section we wish to elucidate these concepts.

An analysis of a tokamak plasma in magnetohydrodynamic equilibrium shows that any point inside of the confined plasma lies on a closed surface of constant pressure that is itself a toroidal surface centered around the toroidal axis (like one of the dashed surfaces drawn in Fig. B.2) [1]. Furthermore, the magnetic field is everywhere tangent to that constant pressure surface. In other words, magnetic field lines are constrained to these surfaces and thus the magnetic flux through them is zero. These surfaces are called flux surfaces. Ignoring drift motion, the guiding center of a particle in the confined plasma remains on a single flux surface. Since the surfaces are nested and do not intersect, they form the convenient radial coordinate scheme described in Section B.1. Furthermore, the largest closed flux surface is precisely the spatial limit of particle confinement; particles radially further away from the toroidal axis will move along field lines that diverge from the torus.

We use some geometric terminology in this paper that may be obscure. First, in a tokamak,

the toroidal axis may be referred to as the plasma axis, and we have done so in the main body of the paper. We use the terminology "outboard side" and "inboard side" of the tokamak to refer to the $\theta = 0$ side and to the $\theta = \pi$ side, respectively. We also discuss the aspect ratio of a tokamak. Referring to Fig. B.1, note that we have two radii: the major radius R and the minor radius a. The ratio R/a is the aspect ratio. Thus a large-aspect-ratio tokamak will have the more familiar donut shape while a small-aspect-ratio tokamak will have only a narrow gap down the center axis. This thesis is primarily focused on NSTX, a small-aspect ratio tokamak.

Bibliography

[1] J. Freidberg, *Plasma Physics and Fusion Energy* (Cambridge University Press, Cambridge, 2007).

[2] E. M. Campbell and W. J. Hogan, "The National Ignition Facility-applications for inertial fusion energy and high-energy-density science," Plasma Physics and Controlled Fusion **41,** B39 (1999).

[3] J. G. Cordey, R. J. Goldsron, and R. R. Parker, "Progress toward a tokamak fusion reactor," Physics Today **45,** 22–30 (1992).

[4] S. Braginskii, "Transport processes in a plasma," Reviews of Plasma Physics **1,** 205 (1965).

[5] P. Helander and D. J. Sigmar, *Collisional Transport in Magnetized Plasmas* (Cambridge University Press, Cambridge, 2002).

[6] M. Taguchi, "Bootstrap current for tokamak plasma with anisotropic electron temperature," Journal of the Physical Society of Japan **65,** 3530–3536 (1996).

[7] M. Ono *et al.*, "Exploration of spherical torus physics in the NSTX device," Nuclear Fusion **40,** 557 (2002).

[8] S. Kaye *et al.*, "Initial physics results from the National Spherical Torus Experiment," Physics of Plasmas **8,** 1977 (2001).

[9] W. Wang, G. Rewoldt, W. Tang, F. Hinton, J. Manickam, L. Zakharov, R. White, and S. Kaye, "Nonlocal neoclassical transport in tokamak and spherical torus experiments," Physics of Plasmas **13,** 082501 (2006).

[10] R. Goldston and P. Rutherford, *Introduction to Plasma Physics* (Institute of Physics Publishing, London, 1995).

[11] M. Taguchi, "Neoclassical transport theory for tokamak plasma with anisotropic temperature in the banana regime," Journal of the Physical Society of Japan **67,** 863–869 (1998).

[12] M. Taguchi, "Effects of temperature anisotropy on neoclassical transport in the plateau and banana-plateau regimes," Journal of the Physical Society of Japan **68,** 97 (1999).

[13] F. Hinton and R. Hazeltine, "Theory of plasma transport in toroidal confinement systems," Reviews of Modern Physics **48,** 239 (1976).

[14] W. Wang, N. Nakajima, M. Okamoto, and S. Murakami, "A new δf method for neoclassical transport studies," Plasma Physics and Controlled Fusion **41,** 1091 (1999).

[15] W. Wang, W. Tang, F. Hinton, L. Zakharov, R. White, and J. Manickam, "Global δf particle simulation of neoclassical transport and ambipolar electric field in general geometry," Computer Physics Communications **164,** 178 – 182 (2004), proceedings of the 18th International Conferene on the Numerical Simulation of Plasmas.

[16] W. Choe, C. Chang, and M. Ono, "Temperature anisotropy in a cyclotron resonance heated tokamak plasma and the generation of poloidal electric field," Physics of Plasmas **2,** 2044 (1995).

Index